Contrib Mineral Petrol (2005) 150: 268–286
DOI 10.1007/s00410-005-0017-8

ORIGINAL PAPER

Daniel E. Harlov · Richard Wirth · Hans-Jürgen Förster

An experimental study of dissolution–reprecipitation in fluorapatite: fluid infiltration and the formation of monazite

Received: 20 September 2004 / Accepted: 1 July 2005 / Published online: 24 September 2005

Abstract In a series of timed experiments, monazite inclusions are induced to form in the Durango fluorapatite using 1 and 2 N HCl and H_2SO_4 solutions at temperatures of 300, 600, and 900°C and pressures of 500 and 1,000 MPa. The monazite inclusions form only in reacted areas, i.e. depleted in (Y + REE) + Si + Na + S + Cl. In the HCl experiments, the reaction front between the reacted and unreacted regions is sharp, whereas in the H_2SO_4 experiments it ranges from sharp to diffuse. In the 1 N HCl experiments, Ostwald ripening of the monazite inclusions took place both as a function of increased reaction time as well as increased temperature and pressure. Monazite growth was more sluggish in the H_2SO_4 experiments. Transmission electron microscopic (TEM) investigation of foils cut across the reaction boundary in a fluorapatite from the 1 N HCl experiment (600°C and 500 MPa) indicate that the reacted region along the reaction front is characterized by numerous, sub-parallel, 10–20 nm diameter nano-channels. TEM investigation of foils cut from a reacted region in a fluorapatite from the 1 N H_2SO_4 experiment at 900°C and 1,000 MPa indicates a pervasive nano-porosity, with the monazite inclusions being in direct contact with the surrounding fluorapatite. For either set of experiments, reacted areas in the fluorapatite are interpreted as replacement reactions, which proceed via a moving interface or reaction front associated with what is essentially a simultaneous dissolution–reprecipitation process. The formation of a micro- and nano-porosity in the metasomatised regions of the fluorapatite allows fluids to permeate the reacted areas. This permits rapid mass transfer in the form of fluid-aided diffusion of cations to and from the growing monazite inclusions. Nano-channels and nano-pores also serve as sites for nucleation and the subsequent growth of the monazite inclusions.

Editorial Responsibility: F. Poitrasson

D. E. Harlov (✉) · R. Wirth · H.-J. Förster
GeoForschungsZentrum Potsdam, Telegrafenberg,
14473 Potsdam, Germany
E-mail: dharlov@gfz-potsdam.de

H.-J. Förster
Institute of Earth Sciences, University of Potsdam,
601553, 14415 Potsdam, Germany

Introduction

The presence of monazite [(Ce,LREE,Th)(PO_4)] and xenotime [(Y,HREE)(PO_4)] associated with apatite [$Ca_{10}(PO_4)_6(F,Cl,OH)_2$] has been demonstrated from natural occurrences (Åmli 1975; Pan et al. 1993; Pan 1997; Harlov et al. 2002a, b) as well as experimentally (Harlov et al. 2002a; Harlov and Förster 2003) to form from the host apatite via the action of fluids. In the apatite structure, (Y + REE) are principally charge balanced through the coupled substitutions:

$$Si^{4+} + (Y + REE)^{3+} = P^{5+} + Ca^{2+} \quad (1)$$

and

$$Na^{+} + (Y + REE)^{3+} = 2\,Ca^{2+} \quad (2)$$

(Pan and Fleet 2002). Various fluids can initiate the removal of Si and/or Na without the coupled removal of (Y + REE). Removal of only Na and Si results in charge imbalance. This frees the (Y + REE) to react with P to form monazite and/or xenotime, either as inclusions in the apatite or as grains on the surface of the apatite. This metasomatically induced origin is supported by the composition of the monazite and/or xenotime, which broadly reflects the (Y + REE + Th + U) abundances in the host apatite. However, the exact composition is dependent on additional parameters such as the chemistry of the metasomatising fluid as well as temperature and pressure (Harlov and Förster 2003). Experimentally, H_2O as well as the H_2O fraction in KCl brines and CO_2/H_2O mixes have been demonstrated as being necessary

for the generation of monazite and xenotime from apatite (Harlov et al. 2002a; Harlov and Förster 2003). This is in comparison to NaCl and $CaCl_2$ brines, which do not promote formation due to the ability of Na^+ and Ca^{2+} to enter the fluorapatite structure, thereby maintaining charge balance should Na^+, Si^{4+} and/or $(Y + REE)^{3+}$ be removed. These experiments also indicate that monazite and xenotime can form over a wide range of temperatures and pressures of, at least, 300–900°C and 500–1,000 MPa. In summary, the fluid chemistry, as well as the (Y + REE) budget available in the apatite, and not pressure and temperature, are the two principal parameters, which facilitate or suppress the formation of monazite and xenotime during apatite–fluid interaction. Consequently, whether or not monazite is associated with (Y + REE)-bearing fluorapatite helps to place constraints on the chemistry of the infiltrating fluids responsible for both the metasomatism of the apatite as well as the rock as a whole.

In this study, investigations into monazite–apatite relationships, begun in Harlov et al. (2002a) and Harlov and Förster (2003), are continued via a series of experiments, which involve reacting the Durango fluorapatite with 1 and 2 N HCl and H_2SO_4 solutions over a wide range of temperatures (300–900°C) and pressures (500–1,000 MPa). The motive for these experiments initially stemmed from speculations concerning the origin of monazite inclusions in fluorapatite from the Kiirunavaara magnetite–fluorapatite ore body, northern Sweden (Harlov et al. 2002b). Therein it was proposed that residual HCl- and/or H_2SO_4-bearing fluids along grain boundaries were involved in the auto-metasomatic formation of monazite inclusions in the fluorapatite shortly after the crystallisation of the ore from a highly evolved, late-stage magma. In this study, experimentally metasomatised regions in the fluorapatite and their monazite inclusions are investigated chemically using electron microprobe analysis (EMP) and examined, on the micron scale, using back-scattered electron (BSE) and scattered electron (SE) imaging as well as, on the nanometre scale, using transmission electron microscopy (TEM), high resolution TEM (HRTEM), and energy dispersive X-ray (EDX) analysis. Comparison is then made with TEM specimens of monazite inclusions in natural fluorapatites from the Kiirunavaara magnetite–fluorapatite ore deposit (Harlov et al. 2002b) and a granulite-facies metabasite from the Ivrea-Verbano zone, N. Italy (Harlov and Förster 2002).

Fluorapatite–fluid experiments

Material for all experiments, as well as material used in characterisation, was taken from a 1 cm long, 0.5 cm wide, light green, euhedral, gem-quality fluorapatite crystal collected at the Kiruna-type magnetite-apatite ore body, Durango, Mexico (Young et al. 1969; Lyons 1988). On the 100 mg scale, ICP-MS trace-element analysis indicates a moderately steep chondrite-normalized (CN) REE pattern ($La_{CN}/Y_{CN} = 21$), a high Th concentration (407 ppm), and a high Th/U ratio of 21 (Harlov and Förster 2003). Microprobe analysis indicates that the 50–100 μm size fluorapatite grains used in the experiments are homogeneous within microprobe error (see below), down to a scale of 3 μm.

The experimental mechanics in this study are similar to those described by Harlov and Förster (2003). This consisted of reacting 20 mg of 20–100 μm size Durango fluorapatite grains with 5 mg of 1 or 2 N HCl and H_2SO_4 solutions at temperatures of 300, 600, and 900°C and pressures of 500 and 1,000 MPa (Table 2). The fluid–mineral ratio was chosen such that it approximated the probable ratio of mobile fluids to fluorapatite present along fluorapatite and magnetite grain boundaries shortly after crystallisation of the Kiirunavaara magnetite–apatite magma. Fluorapatite + acid was loaded into 3 mm wide, 1.3 cm long Pt capsules. After loading, the Pt capsule was pinched shut and then sealed using an argon torch with the capsule partially immersed in an ice water bath.

Experiments at 1,000 MPa and 900°C were done using CaF_2 assemblies. The pressure measured was corrected (+75 MPa) for effects due to friction in the CaF_2 assembly (Harlov and Milke 2002). Both sets of experiments were performed using a two-piston cylinder apparatus as described by Johannes et al. (1971) and Johannes (1973). For each run, two Pt capsules were placed vertically within the assembly such that the NiCr thermocouple tip was located halfway up between the two Pt capsules without touching either. Thermal gradients along the Pt capsules are estimated to be within 20°C. Uncertainty in the pressure is estimated to be ±25 MPa (Harlov and Milke 2002). The experiment was quenched by turning off the current and allowing the H_2O-cooled jacket to cool the bomb. This resulted in temperatures of less than 50°C being reached within 15 s of quench.

Experiments at 500 MPa and 300 and 600°C were performed using a standard cold seal autoclave in conjunction with the hydrothermal apparatus. The internal thermocouple was placed such that the tip was half way up along the Pt capsule. Run times ranged from 1 week to 3 months. Selection of run times was relatively arbitrary though partially dependent on temperature, i.e. lower temperature runs were generally left up longer than higher temperature runs. After the run, the autoclave was quenched using compressed air. Temperatures of 100°C were generally reached within 1–2 min. After the experiment, the Pt capsule was cleaned, weighed, punctured, and dried at 105°C for 6–12 h and then weighed again to determine the fluid content.

Analytical methods

Electron-microprobe analysis

EMP analysis of fluorapatite and monazite were made using the CAMECA SX50 electron microprobe at the

GeoForschungsZentrum Potsdam. Operating conditions, analysis technique, and standards for both apatite and monazite are described in Harlov and Förster (2002). These included a 20 kV, 40 nA, 1–2 μm diameter electron beam for monazite and a 20 kV, 20 nA, 15 μm electron beam spot for the fluorapatite. Primary standards included pure metals for Th and U, vanadinite for Pb, synthetic REE phosphates prepared by Jarosewich and Boatner (1991), synthetic oxides, and natural minerals such as the Durango fluorapatite. Analytical errors for the (Y + REE) in monazite depend on the absolute abundances of each element. Relative errors are estimated to be < 1% at the > 10 wt% level, 5–10% at the 1 wt% level, 10–20% at the 0.2 to 1 wt% level, and 20–40% at the < 0.1 wt% level. For concentrations below 0.1 wt%, the analytical precision for the actinides and lead is much higher, i.e. approximately 10%. Detection limits were approximately 500–1,000 ppm for the (Y + REE), 200–300 ppm for Th and U, and 100 ppm for Pb. EMP measurement of Cl and F in fluorapatite were made according to guidelines outlined in Stormer et al. (1993). High contrast BSE imaging of the monazite grains, coupled with EMP analysis, indicated that they were not zoned with respect to the LREE down to at least 100 ppm which represents the lower limit at which zoning would become visible. Mean EMP analyses of fluorapatite and monazite are contained in Table. 2 and 3, respectively.

EMP traverses, in 3 μm increments across reaction boundaries in the fluorapatite, were made for Ce and Si (oxide wt%) using a 100 nA, 20 kV, 2 μm beam spot (cf. Harlov and Förster 2003). Each spot was measured for 50 s using movable spectrometers. Backgrounds on either side of the peak were counted for 25 s.

Transmission electron microscopy (TEM)

Examples of monazite inclusions in experimentally reacted fluorapatite, i.e. AM34 (600°C; 500 MPa; 1 N HCl) and AM31 (900°C; 1,000 MPa; 1 N H_2SO_4), as well as natural fluorapatite (Ivrea-Verbano Zone), suitable for TEM investigation, were first selected using BSE and SE images. Sampling was accomplished by using focused ion beam (FIB) milling (Wirth 2004). FIB preparation was conducted under ultra-high vacuum conditions in an oil-free vacuum system using a FEI FIB200 instrument at the GeoForschungsZentrum Potsdam. TEM-ready foils of approximately 20×10×0.15 μm representing cross sections of monazite inclusions in reacted fluorapatite, cross sections across reaction fronts, as well as areas deep within reacted and unreacted regions, were cut directly from the fluorapatite grain in the epoxy grain mount by means of a 30 kV Ga-ion beam. The TEM foil was protected from abrasion by the Ga-ion beam by a 1 μm thick Pt layer deposited by using a high-purity organic Pt gas ($C_9H_{16}Pt$, 99.9%), which decomposes in the Ga-ion beam. Once cut, the TEM foils were placed on a perforated carbon film atop a copper grid. Carbon coating to prevent charging in the TEM was not applied.

In the case of monazite inclusions in fluorapatite from the Kiirunavaara magnetite–fluorapatite ore deposit, TEM specimens were extracted from the thin section prepared using a special resin utilised in surface replica techniques, which allows easy extraction of small portions of the thin section. Extraction consisted of first protecting the selected area from damage or deformation with a resin (Technovit, trademark). After extraction, the sample was mounted on a copper grid and the resin dissolved away using acetone. Ion-beam thinning by Ar-ions was performed using a Gatan Duo Mill ion beam thinning machine at 5 kV with a tilt angle of 11 °. The sample was coated slightly with carbon to prevent charging in the TEM.

TEM was carried out in a Philips CM200 instrument operated at 200 kV and equipped with a LaB_6 electron source. Electron energy-loss spectroscopy (EELS) spectra were acquired with a Gatan imaging filter (GIF). Chemical composition was measured using an EDX spectrometer. Analyses were corrected for absorption and fluorescence.

Results

Experimental

In experiments involving HCl as well as H_2SO_4 solutions, a portion of the fluorapatite reacted with the acid, i.e. was metasomatised or changed chemically. Under BSE imaging, reacted regions appear darker relative to unreacted regions due to the depletion of (Y + REE) + Si + Na + S + Cl (Figs. 1, 2, 3, 4; Table. 1, 2). Reacted regions contain monazite inclusions as well as grains of monazite growing along the rim of the reacted fluorapatite (Table 3). Light regions approximate the composition of the unreacted Durango fluorapatite (Table 2) and do not contain inclusions or rim grains of monazite.

In experiments involving HCl, BSE imaging and the EMP traverses indicate that the chemical boundary between the unreacted and reacted regions is compositionally sharp on the micron scale (Figs. 1, 2). In experiment AM33 (900°C; 1,000 MPa; 1 N HCl), monazite grains formed both as inclusions as well as rim grains in sizes ranging from < 1 μm up to 5–10 μm (Fig. 1a, b). Monazite inclusions tend to occur close to or along the boundary between the reacted and unreacted regions in the fluorapatite. In experiment AM34 (600°C; 500 MPa; 1 N HCl), numerous, very small (< 1 μm) monazite grains formed only along the reaction front between the reacted and the unreacted regions (Fig. 1c). Tripling the length of this particular experiment from 3 to 9 weeks (AM46) resulted in a decrease in the number, but an increase in the size of monazite inclusions (Fig. 1d). The relative size of the reacted areas, however, remained unchanged compared to the

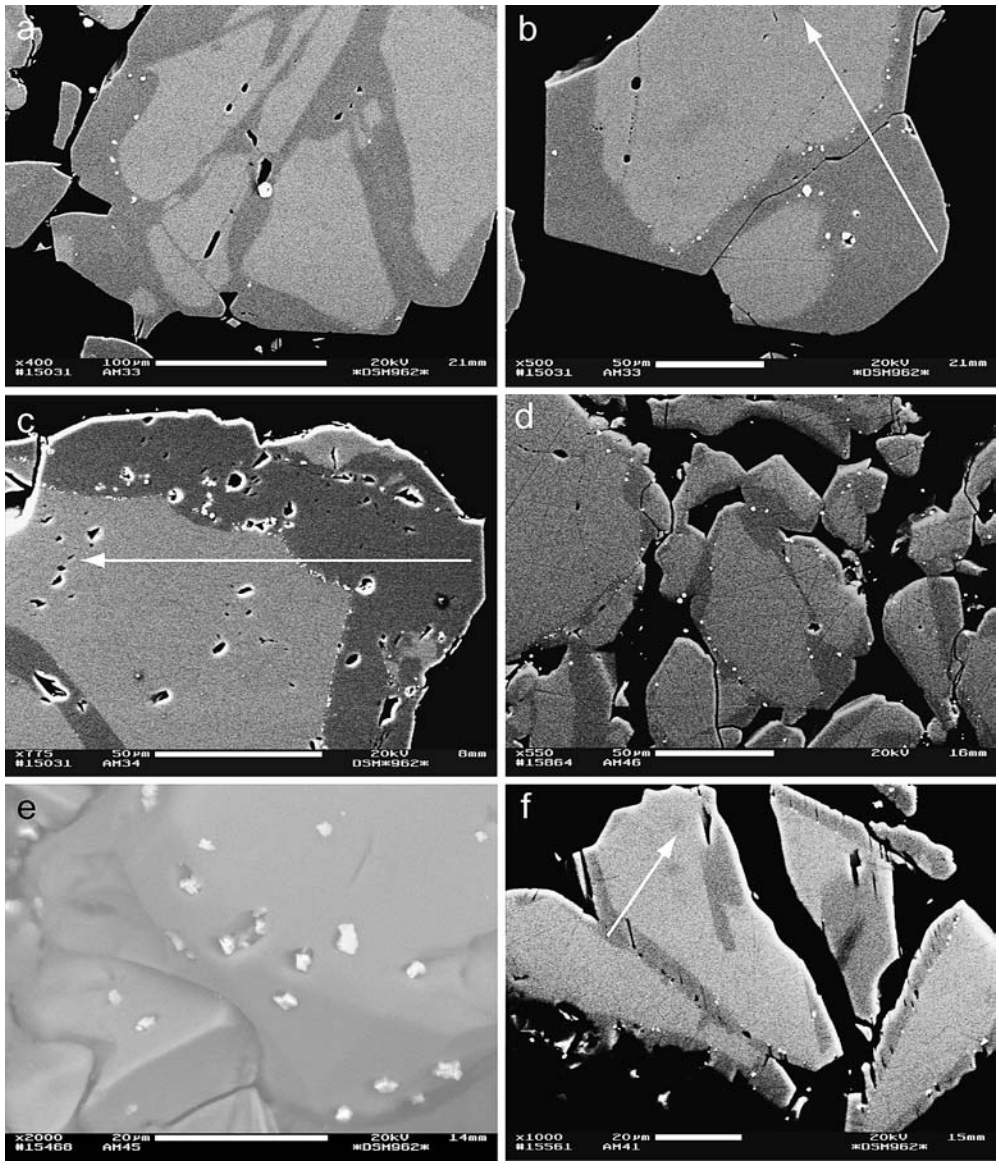

Fig. 1 BSE photographs of fluorapatite reacted with HCl including experiments: **a**, **b** AM33 (900°C; 1,000 MPa; 18 days; 1 N HCl); **c** AM34 (600°C; 500 MPa; 3 weeks; 1 N HCl); **d** AM46 (600°C; 500 MPa; 9 weeks; 1 N HCl); **e** AM45 (600°C; 500 MPa: 7 days; 2 N HCl); and **f** AM41 (300°C; 500 MPa; 14 weeks; 1 N HCl). Dark regions have reacted with the HCl solution and are depleted in (Y + REE) + Si + Na + S + Cl (Table 2), i.e. have been metasomatised. Bright grains are monazite. Analyses of monazite grains in **a** and **b** are tabulated in Table 3. EMP traverses are shown in the figure. The direction of the traverse is indicated by the *arrow*

3-week experiment. Monazite inclusions still occur near or at the reaction front, but also deep within the reacted areas (cf. Figs. 1c, d). Using a 2 N HCl solution (AM45) and leaving the experiment up for a shorter time (7 days), similar dark and light regions formed showing sharp reaction boundaries. Monazite inclusions, similar to that observed in experiment AM33, formed at or near the reaction boundary. In addition, on fluorapatite fracture surfaces, clumps of very small (< 1 μm) monazite crystals are typically surrounded by a partial void (Fig. 1e). Lastly, fluorapatite, reacted with a 1 N HCl solution at 300°C and 500 MPa for 14 weeks (AM41), resulted in porous, dark-reacted regions forming along the rims of the fluorapatite grains, with small (< 2 μm) monazite grains growing in some of the pores (Fig. 1f).

Experiments using 1 and 2 N H_2SO_4 produced broadly similar results (cf. Table. 1, 2; Figs. 3, 4). However, in experiment AM31 (900°C; 1,000 MPa; 1 N H_2SO_4), under BSE imaging, the chemical boundary between the reacted and unreacted fluorapatite ranges from sharp to more diffuse, often in the same grain (e.g. Fig. 3a). An EMP traverse across the sharp reaction boundary shows profiles similar to what is seen in 1 N HCl experiments at 900°C (compare Figs. 2a and 4a). Both elongated (Fig. 3b) and rounded (Fig. 3a) monazite inclusions formed in some of the reacted regions. In experiment AM32 (600°C; 500 MPa; 1 N H_2SO_4), a few, very small, dark-reacted regions developed, along with a few monazite grains. Increasing the concentration of the H_2SO_4 to 2 N (AM44), for the same temperature and pressure, resulted in an increase in the area of the dark-reacted regions as well as the number of monazite inclusions and rim grains (Fig. 3c). Lastly, similar to what was observed at the same pressure and temperature for AM41 in the HCl experiments, experiment AM42 (300°C; 500 MPa; 1 N H_2SO_4; 14 weeks) resulted in

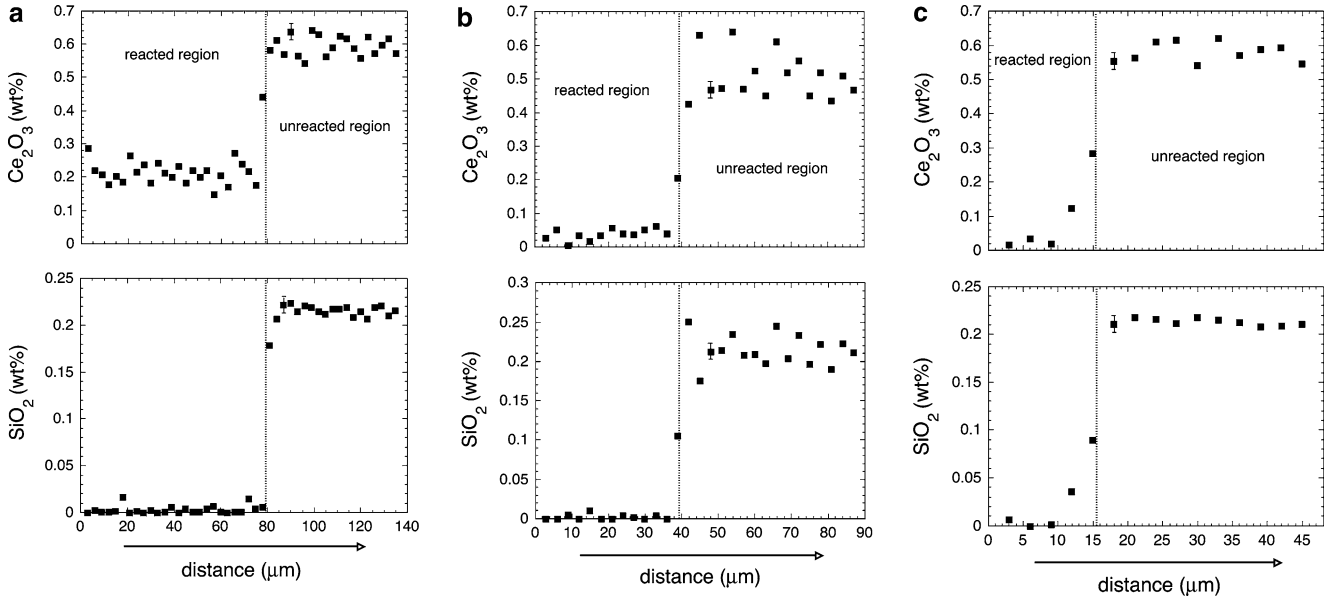

Fig. 2 EMP traverse across reacted and unreacted regions in AM33 (**a**) for the traverse shown in Fig. 1b, in AM34 (**b**) for the traverse shown in Fig. 1c, and in AM41 (**c**) for traverse shown in Fig. 1f. The *dotted line* indicates the approximate boundary between the original fluorapatite and the reacted area. Analysis error is given by an error bar on one of the analysis points

porous-reacted regions along the fluorapatite grain rims (Fig. 3d, e) with a sharp chemical boundary (Fig. 4b).

In most of the experiments, the size of the monazite was too small to obtain EMP analysis data uncontaminated by the reacted fluorapatite host. Compositional data for those monazite grains large enough to be analysed (experiment AM33) are listed in Table 3. The analyses show a relatively small range in the composition of what is a La-rich monazite-(Ce). Their chondrite(CN)-normalized REE patterns are steep ($La_{CN}/Y_{CN} = 84–186$), i.e. significantly steeper than those of the original fluorapatite (average $La_{CN}/Y_{CN} = 21$; Harlov and Förster, 2003). The Th/U ratio ranges around the original fluorapatite average (13–33 vs. 21). The typically low silica contents indicate that only a minor portion of the Th is substituted as huttonite ($ThSiO_4$).

TEM investigation of experiment AM34

TEM foils 1 and 2 were extracted perpendicular to the sharp reaction front separating the reacted and unreacted regions (Fig. 5). TEM foil 3 was extracted deep within the reacted region in AM34, whereas TEM foil 4 was extracted deep within the non-reacted region (Fig. 5).

In TEM foils 1 and 2, the reacted region of the fluorapatite is characterised by a slightly lighter intensity than the unreacted, original fluorapatite (Figs. 6, 7). This is due to the reacted fluorapatite being depleted in both (Y + REE) and Cl compared to the unreacted fluorapatite, thus resulting in a smaller backscattering coefficient $\eta(z,\phi)$ for the reacted region. Here, $\eta(z,\phi)$ is a function of the atomic number z and the tilt angle ϕ. This interface is also confirmed by EDX analysis as well as element mapping, which indicate that the reacted region is depleted in (Y + REE) + Cl compared to the unreacted region. The orientation of the reaction front in both TEM foils 1 and 2 is parallel to the fluorapatite *c*-axis (Figs. 6, 7).

The reacted region in TEM foils 1 and 2 is characterised by several principal features. These include groups of parallel, 5–20 nm wide, hollow, irregular trails of interconnected nano-voids, which might be termed nano-channels. These nano-channels, much like worm trails or ant burrows in dead wood, weave in and out of the plane defined by the TEM foil (cf. Figs. 6b–e, 7a, b). Whereas the interface between the reacted and unreacted fluorapatite is sharply defined on the nanometre scale (Fig. 7c), this boundary, with respect to the nano-channels, is more ragged (e.g. Fig. 6c). Here, a random selection of the nano-channels haphazardly extends across the reaction front into the unreacted fluorapatite. Trails of small fluid inclusions occur in the vicinity of the reaction front (e.g. Fig. 6e). An electron diffraction pattern taken over the reaction front, equally covering the reacted and unreacted fluorapatite in TEM foil 2, indicates that the crystal lattice fringes appear to be continuous across the interface (Fig. 7c). The presence of 2–3 wt % (Y + REE + Si + S + Na + Cl) in the unreacted fluorapatite would imply that the crystal lattice here should be slightly distorted compared to that of the reacted fluorapatite, which is heavily depleted in these elements (cf. Table. 1, 2).

The second principal feature consists of a variety of monazite inclusion types (Figs. 6a, 7a). In general, the monazite inclusions show no preferred orientation with regard to the lattice planes of the fluorapatite. Instead,

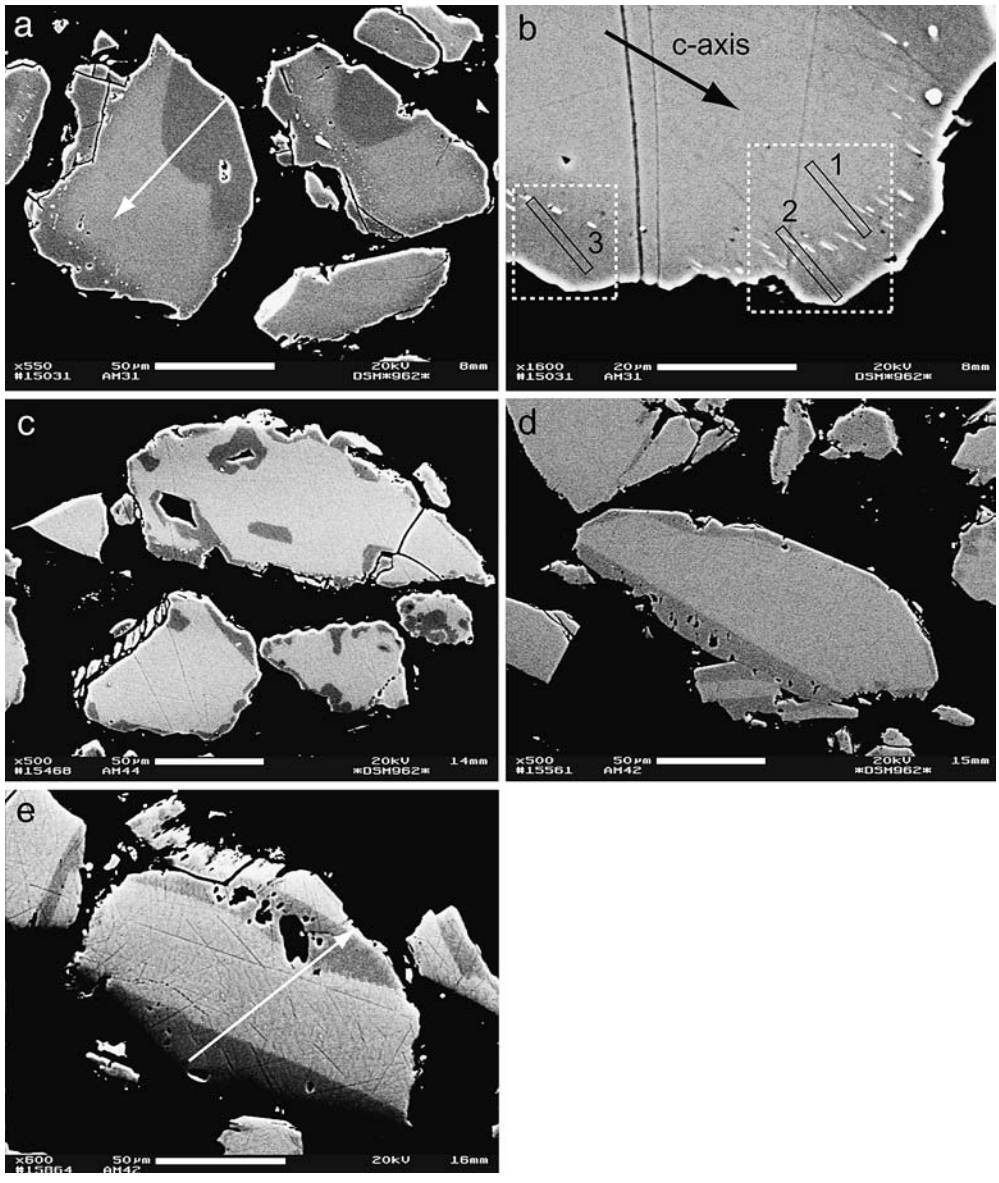

Fig. 3 BSE photographs of fluorapatite reacted with H_2SO_4 including experiments: **a**, **b** AM31 (900°C; 1,000 MPa; 18 days; 1 N H_2SO_4); **c** AM44 (600°C; 500 MPa; 14 days; 2 N H_2SO_4); and **d**, **e** AM42 (300°C; 500 MPa; 14 weeks; 1 N H_2SO_4). Dark regions have reacted with 1 N or 2 N H_2SO_4 and are depleted in (Y + REE) + Si + Na + S + Cl (Table 2), i.e. have been metasomatised. Note that under BSE imaging, some boundaries between the unreacted and reacted regions are diffuse as opposed to sharp indicating some diffusion of (Y + REE) + Si + Na + S + Cl at the reaction boundary. Bright grains are monazite. *Dashed rectangles* in **b** outline the regions in which TEM foils 1, 2, and 3 were sampled. The location and direction of the EMP traverses are indicated by the *white arrows*

they are seen in a variety of textures relative to the surrounding fluorapatite (cf. Figs. 6b–e, 7d). These textures include (a) single monazite grains in direct contact with the fluorapatite (Figs. 6c–e); (b) monazite grains in partial contact with the fluorapatite and partially surrounded by a void filled with an amorphous material (Fig. 6b, e); and (c) clusters of monazite grains at the centre of a void, mostly surrounded by a volatile-rich, amorphous material (Figs. 6b, 7d). This amorphous material represents a quenched fluid/melt(?), in which the monazite grains were apparently growing. EDX analysis indicates that the nominal composition (in wt%) of the quenched material resembles that of a Cl-rich fluorapatite ($P_2O_5 = 37.9$; $CaO = 51.1$; $Cl = 1.0$; $F = 2.1$). However, it is also enriched in LREE ($LREE_2O_3 = 3.7$) and Si ($SiO_2 = 4.8$). HRTEM imaging shows areas of partial dissolution along the margins of the void indicating that as the monazite grains grew, the void was in the process of expanding (Fig. 7e).

Monazite in immediate contact with the fluorapatite, i.e. with no associated void space, could possibly be ascribed as a sampling effect with respect to the cutting of TEM foil 1. However, the last two monazite inclusions along the reaction front in Figs. 6d and e are partially in contact with a large void connecting the two with a very small void at the lower end of the last monazite inclusion. This could represent some sort of evolutionary state with regard to how the monazite grains interact with the surrounding voids and fluorapatite over time. That is, monazite growth eventually outstrips nano-void growth such that the monazite grain fills or nearly fills in the void. While these monazite inclusions tend to occur right at the reaction front (Fig. 6a), they are also found in the (Y + REE)-depleted region, behind the reaction front (Fig. 7a). In either case, these inclusions are wholly surrounded by dense agglomerations of nano-channels (Figs. 6b, e, 7d). These nano-channels are either at apparent right angles to

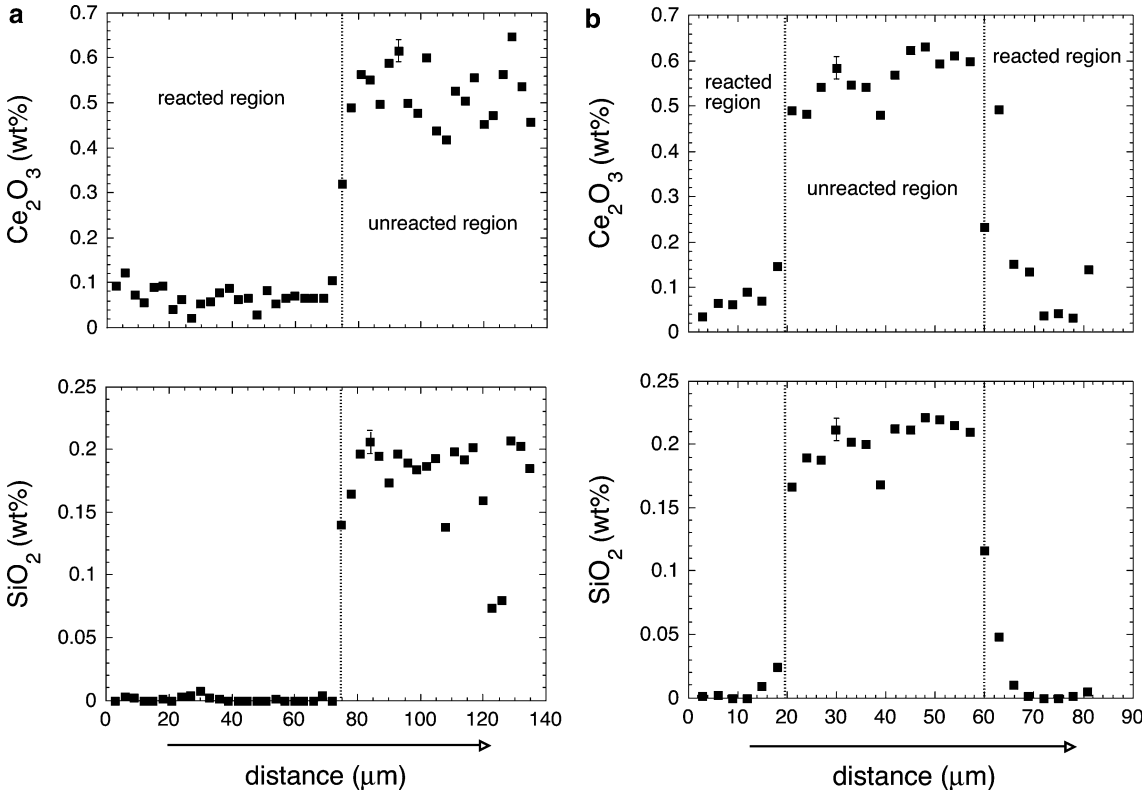

Fig. 4 EMP traverse across reacted and non-reacted regions in AM31 (**a**) for the traverse shown in Fig. 3a, and in AM42 (**b**) for the traverse shown in Fig. 3e. The *dotted line* indicates the approximate boundary between the original fluorapatite and the reacted fluorapatite. Analysis error is given by an error bar on one of the analysis points

other nano-channels (Fig. 7a), or parallel to them (Fig. 6b).

A difference is seen in electron energy loss (EEL) spectra taken of the unreacted and the reacted fluorapatite (Fig. 8). While both EEL spectra indicate the same approximate intensity for the oxygen and fluorine K-edge, the EEL spectrum for the reacted fluorapatite also shows a pre-peak at about 528 eV, which is indicative of OH (Wirth 1997). This can be attributed to OH replacing F on the halogen site in the fluorapatite structure, since any free H_2O present in the nano-channels most likely would have been lost either during the cutting of the foil or during the bombardment of the foil with high-energy electrons during TEM.

Cut deep within the reacted region in the fluorapatite, TEM foil 3 shows no evidence of nano-channels, nano-voids, or monazite inclusions (Fig. 9). Rather, under HRTEM, it is characterised by a mottled contrast. This is indicative of slightly mis-oriented crystal segments (mosaic crystal) and is most likely due to the healing of the nano-voids and nano-channels. This pattern contrasts strongly with TEM foil 4 cut deep within the non-reacted fluorapatite (Fig. 10). Here, no mottling of the lattice fringes is seen. Such an HRTEM image is typical of the original fluorapatite crystal lattice before having undergone dissolution–reprecipitation.

TEM investigation of experiment AM31

Three TEM foils were extracted in the reacted area along the rim of the fluorapatite grain, approximately parallel to the fluorapatite *c*-axis (cf. Fig. 3b). In TEM foils 2 and 3, the monazite inclusions are in direct contact with the surrounding fluorapatite filling the original voids in such a way that their shape approximates that of fluorapatite (Figs. 11, 12). TEM foil 2, cut close to the edge of the fluorapatite grain, shows groups of semi-parallel nano-void channels, along with monazite inclusions (Fig. 11). TEM foil 3, cut further into the diffuse boundary between the reacted and unreacted regions, displays numerous, individual nano-voids, randomly though evenly distributed throughout the reacted fluorapatite (Fig. 12a). These nano-voids, under HRTEM, tend to exhibit a negative hexagonal crystal symmetry (Fig. 12b). They are also present in areas containing nano-channels (cf. upper left-hand corner in Fig. 11a). TEM foil 1, cut in the region of the diffuse boundary between the reacted and unreacted regions, samples one of the elongated monazite inclusions. This inclusion appears to be growing into a void, presumably once fluid-filled, which is orientated parallel to the fluorapatite *c*-axis (Fig. 13a). However, along the sides of the inclusion perpendicular to the *c*-axis, the monazite is

Table 1 Compilation of experimental results

Exp	*P* (MPa)	*T* (°C)	Fluid	Time (days)	Results
AM33	1,000	900	1 N HCl	18	Scattering of (1–10) μm monazite inclusions in areas depleted in (Y + REE) + Si + Na + S + Cl. Inclusions are generally found near and/or along the sharp reaction boundary dividing the reacted from the unreacted fluorapatite. Occasional rim grains of monazite (5–10 μm) are found on the edge of fluorapatite grains in the reacted areas.
AM34	500	600	1 N HCl	21	Reacted areas are depleted in (Y + REE) + Si + Na + S + Cl. Numerous very small (< 1 μm) monazite inclusions outline the sharp reaction boundary dividing the reacted from the non-reacted fluorapatite.
AM46	500	600	1 N HCl	63	Reacted areas are depleted in (Y + REE) + Si + Na + S + Cl. Scattering of small to medium (1–5 μm) monazite inclusions in the reacted areas. These partially outline the sharp reaction boundary separating the reacted from the non-reacted fluorapatite.
AM45	500	600	2 N HCl	7	Reacted areas are depleted in (Y + REE) + Si + Na + S + Cl. Numerous, very small (< 1 μm) monazite inclusions outline the sharp reaction boundary dividing the reacted from the non-reacted fluorapatite. Also seen are a scattering of small monazite inclusions (1–2 μm) in the reacted regions near the reaction boundary.
AM41	500	300	1 N HCl	98	Reacted areas are depleted in (Y + REE) + Si + Na + S + Cl and characterised by micro-pores (1–5 μm), about half of which are elongated with respect to the fluorapatite *c*-axis. Scattering of small (1 μm) monazite inclusions in the reacted regions outline the sharp reaction boundary separating the reacted from the non-reacted fluorapatite. Monazite inclusions (1μm) are found within the reacted areas as well as on the surface of the micro-pores.
AM31	1,000	900	1 N H_2SO_4	18	Reacted areas are depleted in (Y + REE) + Si + Na + S + Cl. A scattering of monazite inclusions (< 1–2 μm), both round and elongated, are found within the reacted regions as well as sometimes partially outlining the reaction boundary separating the reacted from the non-reacted fluorapatite. Elongated monazite inclusions are parallel to the fluorapatite *c*-axis. Under BSE imaging, the reaction boundary ranges from diffuse to sharp.
AM32	500	600	1 N H_2SO_4	21	A very few very small reacted regions depleted in (Y + REE) + Si + Na + S + Cl formed along the fluorapatite grain rims. A sharp reaction boundary separates the reacted from the non-reacted fluorapatite. A very few, small (1 μm) monazite inclusions are found in the reacted regions.
AM44	500	600	2 N H_2SO_4	14	Reacted areas, depleted in (Y + REE) + Si + Na + S + Cl, formed along the fluorapatite grain rims. A few small (1 μm) monazite inclusions are found in the reacted areas. A sharp reaction boundary separates the reacted from the non-reacted fluorapatite.
AM42	500	300	1 N H_2SO_4	98	Reacted areas are depleted in (Y + REE) + Si + Na + S + Cl and characterised by micro-pores (1-5 μm), a third of which are elongated with respect to the fluorapatite *c*-axis. A few small (< 1–1 μm) monazite grains are found in the reacted regions, mostly within the micro-pores.

in direct contact with the fluorapatite host, with no evidence of an amorphous layer separating the monazite from the fluorapatite. At the end of the void, a transition region is seen, which is characterised by preferred dissolution along the fluorapatite *c*-axis in the form of a crown of small, spike-like needles less than 5 nm in diameter (Fig. 13b). The main body of the reacted fluorapatite surrounding the monazite inclusions is characterised by numerous, evenly distributed small nano-voids with an inverted hexagonal symmetry similar to those seen in Fig. 12.

TEM investigation of two natural examples

For the purpose of comparison, two natural examples of monazite inclusions in fluorapatite were also investigated. These included fluorapatite from the Kiirunavaara magnetite–apatite ore deposit, N. Sweden (Harlov et al. 2002b) and from a granulite-facies metabasite in the Val Strona area of the Ivrea-Verbano Zone, N. Italy (Harlov and Förster 2002).

In the Kiirunavaara fluorapatite, the monazite inclusions are surrounded by an apparent amorphous rim (Fig. 14). EDX analysis indicates that this rim is enriched in elements incompatible with both monazite and fluorapatite such as Si and Mg, while being heavily depleted in P, Ca, and (Y + REE). This supports the idea that the amorphous rim is not an artefact from the argon-milling process. This, and the similarity between such amorphous rims and the fluid-filled voids in which some of the monazite grains grew in the HCl experiments (e.g. Figs. 6b, 7d), would support the conjecture proposed by Harlov et al. (2002b). Namely that fluorapatite in the Kiirunavaara ore deposit experienced autometasomatism due to residual, acid-rich fluids, perhaps

Table 2 EMP analyses (wt%) of experimentally metasomatised fluorapatite

Exp	*P* (MPa)	*T* (°C)	Fluid	Time (days)	Area	P_2O_5	SiO_2	SO_3	Y_2O_3	La_2O_3	Ce_2O_3	Nd_2O_3	CaO	MnO	FeO[a]	SrO	Na_2O	F	Cl	H_2O[b]	Sum	O=(F+Cl)	Total	$(Y+REE)_2O_3$
Durango fluorapatite crystal used in this study						40.7	0.48	0.30	0.07	0.51	0.67	0.18	54.10	0.01	0.03	0.07	0.20	3.39	0.41	0.06	101.13	1.52	99.61	1.43
						0.28	*0.03*	*0.05*	*0.02*	*0.07*	*0.07*	*0.04*	*0.20*	*0.01*	*0.02*	*0.03*	*0.02*	*0.06*	*0.03*	*0.03*				
AM33	1000	900	1 N HCl	18	Dark	42.14		0.01		0.16	0.25	0.14	54.85	0.01	0.01	0.08	0.01	3.83	0.32		101.82	1.69	100.13	0.55
						0.30		*0.02*		*0.06*	*0.07*	*0.06*	*0.18*	*0.02*	*0.02*	*0.02*	*0.01*	*0.22*	*0.01*					
					Light	40.96	0.47	0.26	0.07	0.54	0.74	0.25	53.81	0.01	0.04	0.05	0.25	3.90	0.39		101.71	1.73	99.98	1.60
						0.16	*0.03*	*0.02*	*0.02*	*0.04*	*0.08*	*0.03*	*0.10*	*0.01*	*0.05*	*0.01*	*0.02*	*0.32*	*0.03*					
AM34	500	600	1 N HCl	21	Dark	42.20		0.02			0.05		55.07	0.01	0.04	0.06	0.04	3.89	0.24		101.61	2.11	99.50	0.05
						0.13		*0.02*			*0.04*		*0.15*	*0.01*	*0.04*	*0.02*	*0.01*	*0.29*	*0.05*					
					Light	40.72	0.47	0.22	0.06	0.55	0.69	0.16	53.69	0.01	0.06	0.06	0.25	3.84	0.42		101.20	1.71	99.49	1.45
						0.25	*0.02*	*0.04*	*0.02*	*0.07*	*0.08*	*0.04*	*0.11*	*0.01*	*0.04*	*0.02*	*0.02*	*0.32*	*0.01*					
AM46	500	600	1 N HCl	63	Dark	42.27	0.02	0.02			0.08		55.44	0.01	0.01	0.08	0.02	3.71	0.29		101.93	1.62	100.31	0.08
						0.21	*0.02*	*0.02*			*0.05*		*0.21*	*0.02*	*0.01*	*0.02*	*0.02*	*0.24*	*0.03*					
					Light	41.43	0.32	0.34	0.02	0.49	0.56	0.14	54.20	0.01	0.04	0.07	0.26	3.62	0.41		101.92	1.62	100.30	1.21
						0.19	*0.03*	*0.07*	*0.02*	*0.07*	*0.05*	*0.04*	*0.12*	*0.02*	*0.03*	*0.02*	*0.03*	*0.08*	*0.02*					
AM45	500	600	2 N HCl	7	Dark	42.29	0.02	0.02	0.04	0.05	0.15	0.05	55.23	0.02	0.02	0.07	0.01	3.76	0.28		102.01	1.65	100.36	0.29
						0.20	*0.02*	*0.02*	*0.02*	*0.04*	*0.05*	*0.04*	*0.31*	*0.02*	*0.02*	*0.03*	*0.01*	*0.09*	*0.03*					
					Light	41.40	0.40	0.21	0.07	0.54	0.66	0.18	54.12	0.02	0.03	0.04	0.18	3.68	0.39		101.94	1.64	100.30	1.46
						0.09	*0.02*	*0.03*	*0.03*	*0.06*	*0.08*	*0.04*	*0.21*	*0.02*	*0.02*	*0.02*	*0.02*	*0.20*	*0.01*					
AM41	500	300	1 N HCl	98	Dark	42.29	0.02						55.30	0.02		0.05	0.01	3.99	0.09		101.78	1.70	100.08	0.00
						0.20	*0.02*						*0.30*	*0.02*		*0.03*	*0.02*	*0.24*	*0.02*					
					Light	41.53	0.40	0.20	0.08	0.56	0.64	0.19	53.86	0.01	0.03	0.04	0.16	3.85	0.38		101.94	1.71	100.23	1.47
						0.19	*0.03*	*0.05*	*0.02*	*0.11*	*0.09*	*0.08*	*0.19*	*0.01*	*0.02*	*0.03*	*0.03*	*0.18*	*0.02*					
AM31	1000	900	1 N H_2SO_4	18	Dark	42.29		0.05		0.08	0.12	0.09	54.94	0.02	0.06	0.08	0.03	3.84	0.19		101.79	1.66	100.13	0.29
						0.19		*0.02*		*0.04*	*0.03*	*0.03*	*0.19*	*0.01*	*0.04*	*0.03*	*0.01*	*0.21*	*0.01*					
					Light	41.33	0.47	0.23	0.06	0.56	0.67	0.20	53.59	0.01	0.06	0.07	0.23	3.65	0.25		101.37	1.59	99.78	1.49
						0.20	*0.04*	*0.04*	*0.02*	*0.08*	*0.07*	*0.05*	*0.16*	*0.01*	*0.04*	*0.02*	*0.03*	*0.23*	*0.03*					
AM32	500	600	1 N H_2SO_4	21		41.17	0.45	0.22	0.07	0.51	0.69	0.21	53.58		0.06	0.05	0.23	3.71	0.37		101.31	1.65	99.66	1.47
						0.24	*0.02*	*0.02*	*0.02*	*0.06*	*0.07*	*0.05*	*0.21*		*0.04*	*0.03*	*0.02*	*0.21*	*0.02*					
AM44	500	600	2 N H_2SO_4	14	Dark	42.30	0.03	0.02			0.07		55.54	0.01	0.07	0.08	0.01	3.98	0.10		102.22	1.70	100.52	0.07
						0.17	*0.02*	*0.02*			*0.03*		*0.13*	*0.02*	*0.04*	*0.03*	*0.02*	*0.18*	*0.03*					
					Light	41.34	0.42	0.21	0.07	0.55	0.70	0.21	54.16	0.02	0.04	0.04	0.19	3.74	0.38		102.06	1.66	100.40	1.53
						0.20	*0.02*	*0.04*	*0.02*	*0.05*	*0.06*	*0.08*	*0.26*	*0.02*	*0.03*	*0.03*	*0.02*	*0.18*	*0.02*					
AM42	500	300	1 N H_2SO_4	98	Dark	42.33	0.03	0.02			0.05		55.37	0.02	0.01	0.05	0.01	3.89	0.02		101.80	1.64	100.16	0.05
						0.28	*0.03*	*0.02*			*0.03*		*0.44*	*0.02*	*0.02*	*0.01*	*0.01*	*0.20*	*0.02*					
					Light	41.36	0.44	0.20	0.09	0.55	0.65	0.22	54.06	0.03	0.04	0.05	0.18	3.79	0.39		102.05	1.68	100.37	1.51
						0.14	*0.02*	*0.04*	*0.02*	*0.06*	*0.05*	*0.06*	*0.13*	*0.02*	*0.02*	*0.04*	*0.03*	*0.13*	*0.02*					

1-σ standard deviation in italicsBlank = below EMP detection limit

[a]Total Fe as FeO

[b]Calculated to be 0 assuming the (F,Cl,OH) site is filled

Table 3 EMP analyses (wt%) of monazite from AM33

	1	2	3	4	5	6	7	8
P_2O_5	30.39	30.36	30.54	29.76	30.57	30.49	30.49	30.36
SiO_2	0.09	0.08	0.10	0.41	0.08	0.08	0.08	0.07
ThO_2	3.02	2.96	2.78	2.59	2.44	2.30	2.05	1.85
UO_2	0.21	0.14	0.13	0.20	0.07	0.15	0.09	0.12
Y_2O_3	1.00	1.60	1.79	1.34	1.63	1.06	1.64	2.08
La_2O_3	25.70	23.97	23.82	24.76	24.41	26.29	24.58	24.14
Ce_2O_3	29.12	28.43	29.07	28.51	28.74	29.81	29.29	29.12
Pr_2O_3	1.78	1.87	1.94	1.87	1.93	1.85	1.95	1.93
Nd_2O_3	5.80	6.39	6.60	5.96	6.67	6.01	6.48	6.79
Sm_2O_3	0.63	0.67	0.65	0.72	0.82	0.55	0.77	0.80
Gd_2O_3	0.52	0.71	0.63	0.63	0.62	0.59	0.66	0.69
Tb_2O_3	0.10	0.12	0.07			0.08	0.10	
Dy_2O_3	0.10	0.29	0.24	0.17	0.40	0.14	0.23	0.28
Er_2O_3		0.17	0.15	0.14	0.19	0.07	0.15	0.16
CaO	0.95	1.98	1.40	1.85	1.47	0.98	1.18	1.39
Total	99.46	99.83	99.97	98.91	100.16	100.48	99.75	99.82
La_{CN}/Y_{CN}	186	108	96	133	108	178	108	84
Th/U	14	21	22	13	33	15	22	16

Blank = below EMP detection limit

dominated by HCl, present along grain boundaries shortly after the end of crystallisation.

Monazite inclusions, which lack an amorphous rim and instead are mostly in direct contact with the surrounding mineral, are observed in fluorapatite from the Ivrea-Verbano zone sample (Fig. 15). Here, KCl-rich brines are proposed to have initiated dehydration of the metabasites from amphibolite grade to orthopyroxene-bearing granulite grade and, at the same time, induced formation of monazite inclusions in the fluorapatite. This has been confirmed experimentally by Harlov and Förster (2003).

While mostly in direct contact with the surrounding fluorapatite, occasional voids are seen randomly distributed along the monazite–fluorapatite grain boundary interface (Fig. 15b). Such voids could be the remnants of amorphous layers partially recrystallised during post-peak metamorphic uplift and cooling, or they could represent a preserved feature concurrent with monazite inclusion growth. The latter interpretation is supported by the fact that they show some similarity with the partial voids seen along the monazite–fluorapatite grain boundary interface in Fig. 6e. This would suggest that they represent regions in the original void space not filled in by the growing monazite grain. In either the Kiirunavaara or Ivrea-Verbano zone samples, any evidence of nano-channels or a nano-porosity has most likely long since disappeared due to recrystallisation of the fluorapatite during metamorphic uplift and cooling.

Discussion

HCl reaction experiments

The relatively sharp textural and chemical boundary between the reacted and unreacted regions (Figs.1, 2, 3, 4), the mosaic crystal pattern, i.e. healed crystallographic lattice, deep within the reacted areas, and the nano- and micro-porosity still present in the vicinity of the reaction boundary, implies that the principal mechanism responsible for the formation of the reacted regions was dissolution–reprecipitation, as opposed to volume diffusion (Putnis 2002). This mechanism is fur-

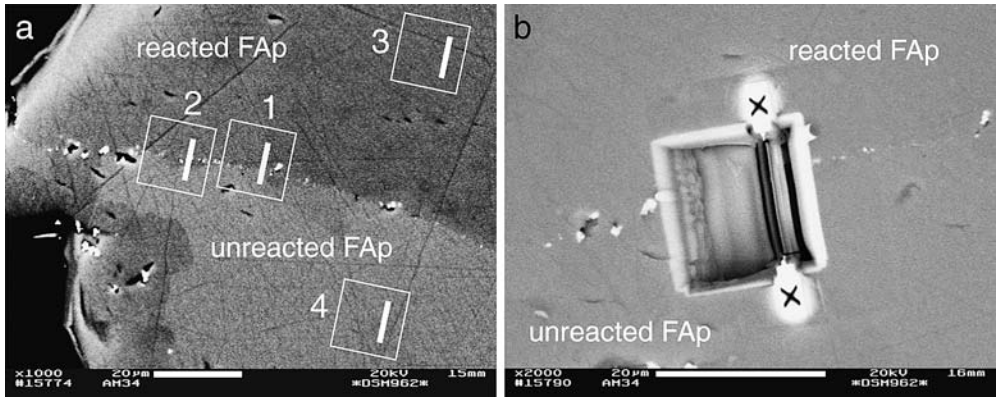

Fig. 5 **a** shows a BSE photograph of a fluorapatite grain from experiment AM34 and indicates the exact locations where TEM foils 1, 2, 3, and 4 were sampled. **b** shows a close-up of the area where TEM foil 2 was cut and later removed. The exact location of the foil was between the two x marks

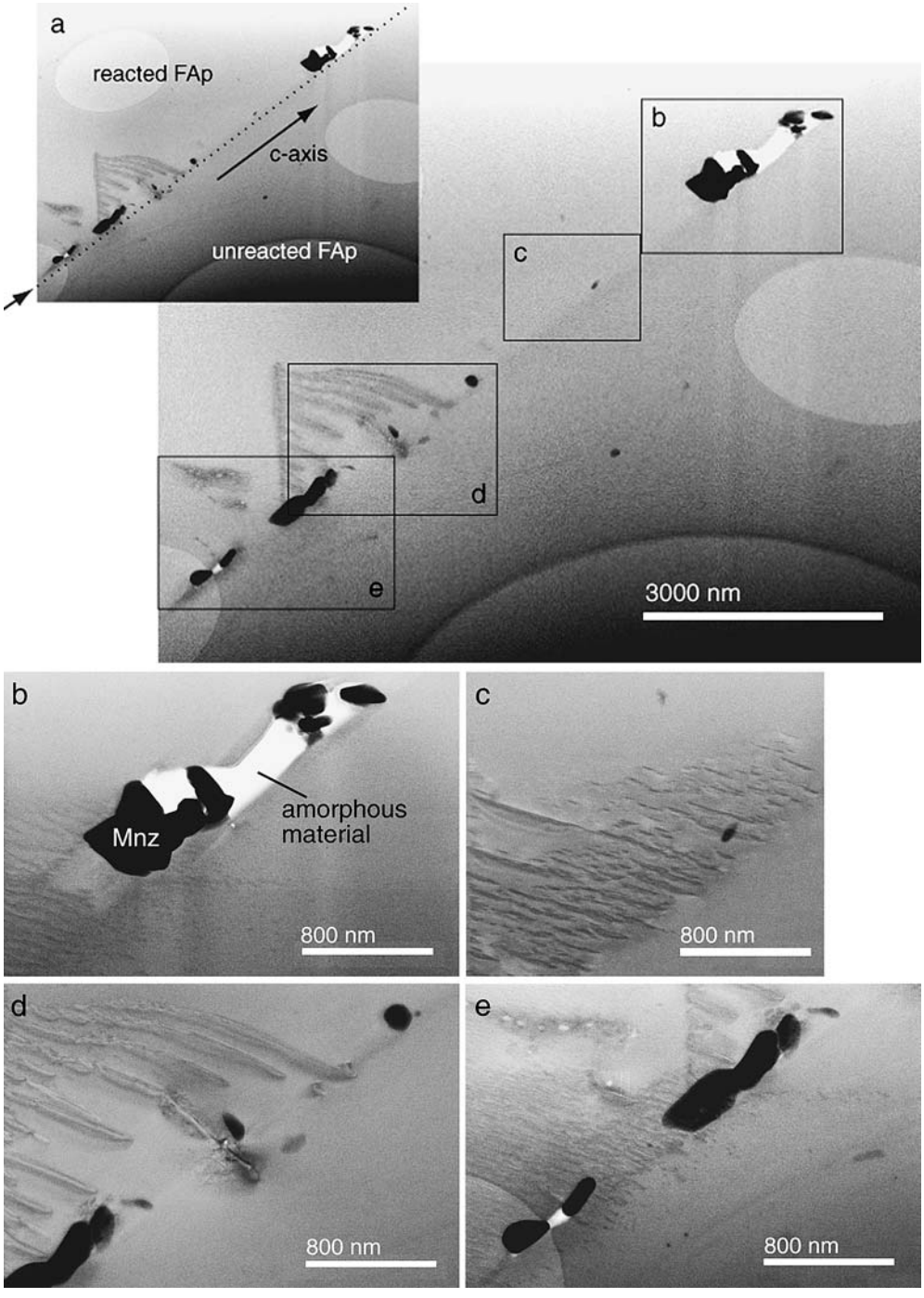

Fig. 6 **a** shows TEM foil 1 from experiment AM34 as sampled across the reaction front shown in Fig. 5a . *Large, elongate circles* reflect holes in the carbon substrate upon which the foil rests. Darkening towards the bottom of the foil is indicative of a slight thickening towards the base as well as possible increase in Ga contamination since the base of the foil was cut using the Ga-ion beam. In the upper left-hand inset, the reaction or infiltration front is indicated by a *dotted line* and *arrow*. Dark monazite grains are seen growing along the reaction front. Specific textures along the reaction front are delineated by *lettered boxes*. **b** shows several clusters of monazite grains in a void filled by a fluid-rich quenched melt. Note the delicate nano-channels in the lower left-hand corner of the picture. These nano-channels are seen in much greater detail in (**c**), where they end somewhat raggedly at the reaction front partially crossing it. Comparatively coarser nano-channels are seen in (**d**); one or two of which appear to cross the reaction front. The monazite inclusions along the reaction front in this figure are not associated with any type of void and show direct contact with the fluorapatite (see also small monazite inclusions in **c**). In overlapping **e**, nano-channels are seen at the same approximate angle to the reaction front as seen in **b**–**d**. Again, note the ragged edge of the nano-channels along the reaction front, some of whom partially cross it. In addition, there is a trail of small fluid inclusions in the upper left-hand corner. The monazite inclusion clump in the upper half of the figure shows apparent contact with the surrounding fluorapatite, whereas the two monazite grains in the lower half are partially surrounded by an amorphous region

ther confirmed by the fact that the diffraction pattern of the reacted, i.e. depleted region, appear to be nearly identical with those of the unreacted fluorapatite (Fig. 7c). This implies that the reacted and unreacted parts of the fluorapatite still consist of one single crystal. The role that the interconnected nano-pores and nano-channels play in the reacted regions with regard to fluid-aided mass transfer is clearly seen by the presence of monazite grains in voids within the reacted region (Figs. 6b, 7d). Fluids in the nano-channels allow for the rapid transfer of cations both to and from the growing monazite grains as evidenced by the REE-rich composition of the quenched amorphous material in these voids. Phosphorous, obtained locally from the progressive dissolution of the walls of the void with subsequent fluid-aided removal of Ca (probably as $CaCl_2$), would allow for the expansion of the void as the monazite crystals grew in size. REE would probably complex as salts, thereby enhancing their solubility. Why a build up of Si is also observed could be due to the fact that unless there are (Y + REE) present in the fluorapatite structure to maintain charge balance, Si will be expelled into the solution present in the nano-channels. In this case, creation and growth of the monazite inclusions will use up the (Y + REE) throughout the reacted region leaving the incompatible Si behind to build up in the amorphous material. Silicon could only be taken into the monazite in the form of the huttonite component, i.e. $ThSiO_4$, which, in these experiments, did not occur to any great extent (cf. Table 3). In contrast, this was the case in brine experiments also utilizing the Durango fluorapatite as described in Harlov and Förster (2003).

The fact that the depleted fluorapatite, deep with in the reacted region, does not possess a pervasive nano-porosity or nano-channels (cf. Fig. 9) can be explained as a consequence of the subsequent healing and partial recrystallisation of the crystal lattice. Only the considerably lower reactivity of the 1 N H_2SO_4 solution with fluorapatite, as opposed to the 1 N HCl solution, could explain the abundant nano-porosity still prevalent in AM31 at 900°C and 1,000 MPa (Figs. 11, 12, 13). In contrast, much lower temperatures, i.e. 300°C, and extended time, i.e. 14 weeks, allowed for the nano-porosity to evolve into a micro-porosity and thus, be preserved as seen in experiments involving both HCl (AM41; Fig. 1f) and H_2SO_4 (AM42; Fig. 3d, e). Monazite inclusions without amorphous rims could represent a second type of evolutionary

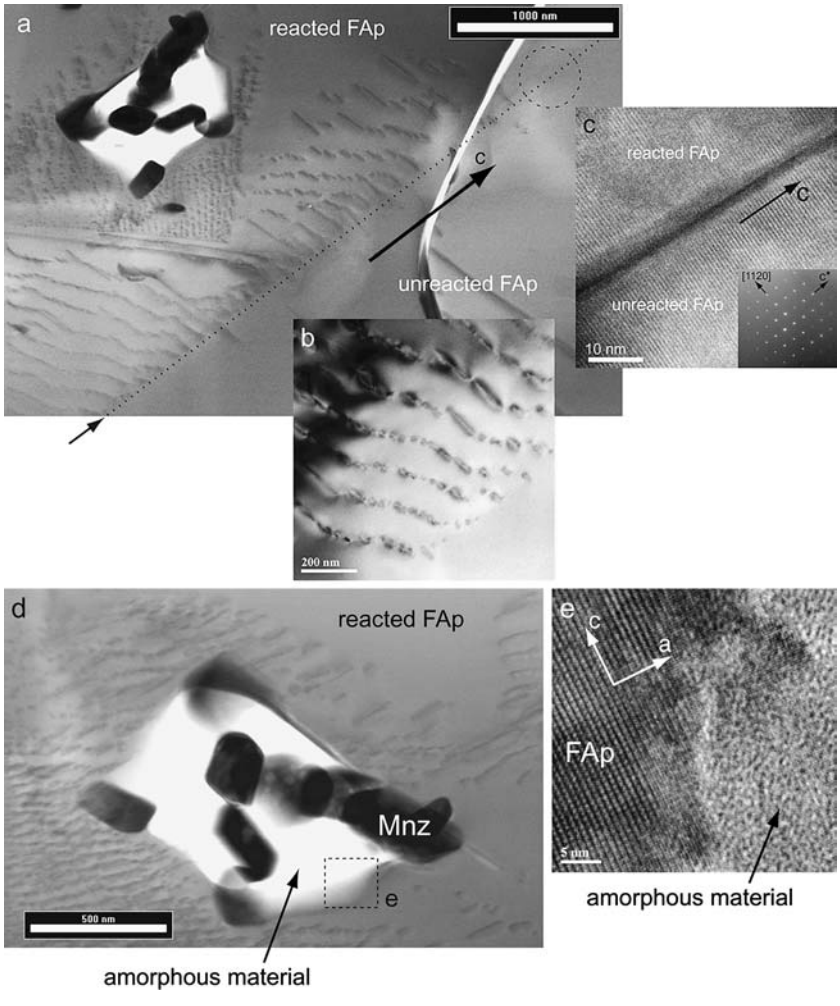

Fig. 7 **a** shows a series of sub-parallel nano-channels and a group of monazite grains in a cavity filled with an amorphous quenched material. The photo is taken from a region of TEM foil 2 (AM34) located at the boundary between the reacted and unreacted fluorapatite (*dotted line* and *arrow*) (cf. Fig. 5a, b). A close-up of the nano-channels is shown in (**b**). **c** shows a lattice fringe image of the interface between the reacted and the unreacted fluorapatite taken from the region within the *dashed circle*. **d** shows a close-up of the void, which is filled with a quenched amorphous fluid and a cluster of monazite grains. The void is surrounded by an array of nano-channels. **e** shows an HRTEM image along the void rim with an irregular interface

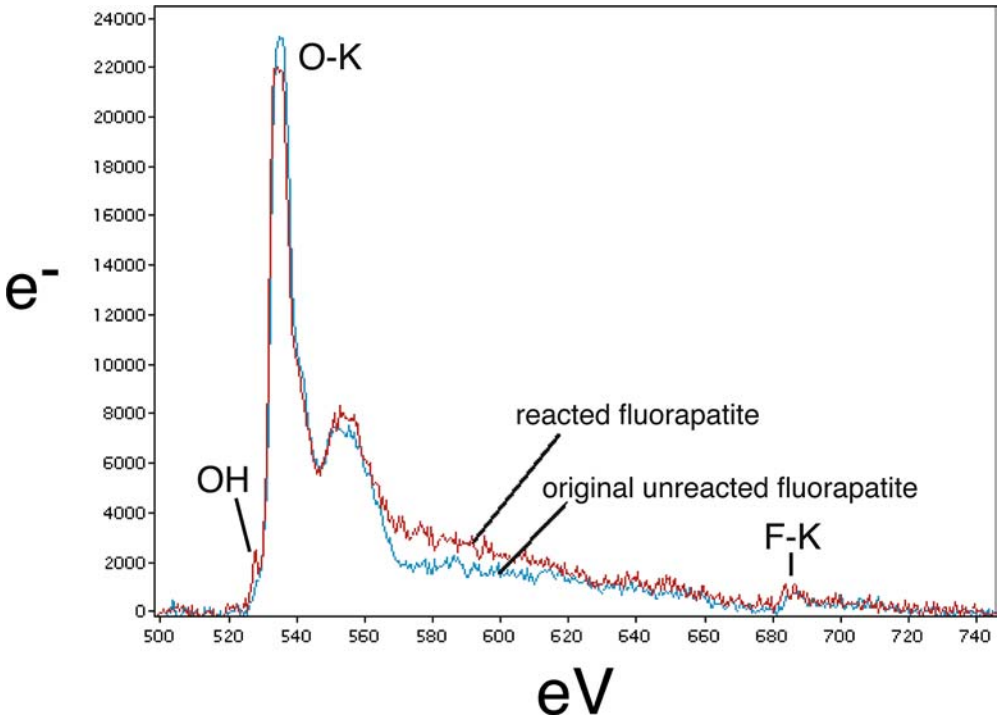

Fig. 8 EEL spectra of the reacted fluorapatite, i.e. Y + REE-depleted, and the unreacted fluorapatite. The oxygen K-edge shows a pre-peak at about 528 eV, which is an indication for OH. This pre-peak is absent in the spectrum of the unreacted fluorapatite

stage, where the growth of the monazite outstrips the dissolution of the surrounding fluorapatite such that the monazite grain has filled in the void space thereby coming into direct contact with the fluorapatite.

Formation of monazite inclusions along or in the immediate vicinity of the reaction front, as seen in the HCl experiments, suggests that the (Y + REE) experienced an effect somewhat analogous to that of a chromatographic column. In such a scenario, the (Y + REE) are concentrated principally at the reaction front as the reacted region expands in size via dissolution–reprecipitation over the course of the experiment. Simultaneously, behind the moving reaction front, the reacted region is progressively recrystallised, starting at

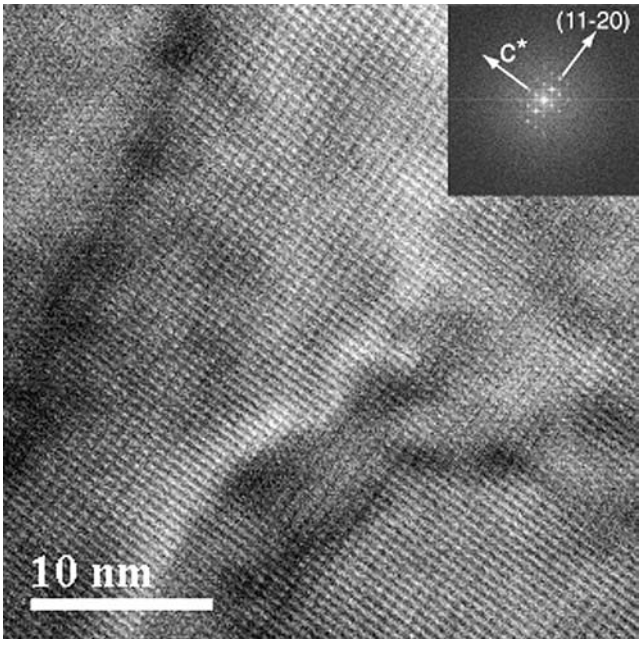

Fig. 9 HRTEM image of a fluorapatite from a reacted region in experiment AM34 (cf. Figs. 1c, 5a)

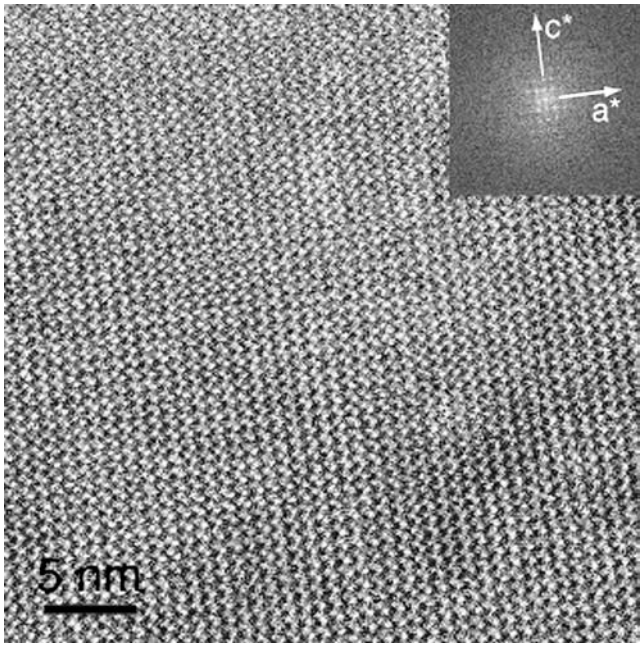

Fig. 10 HRTEM image of a non-reacted region, i.e. the original fluorapatite, in experiment AM34 (cf. Figs. 1c, 5a)

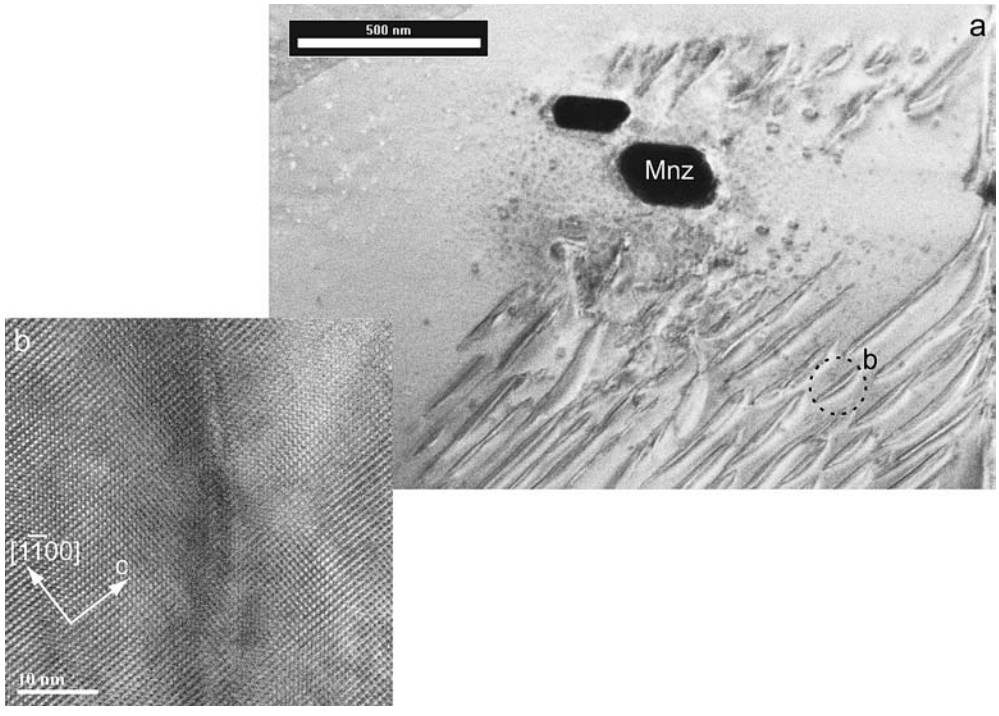

Fig. 11 **a** shows a TEM bright field image taken from foil 2 (AM31; Fig. 3b) of sub-parallel nano-void channels and monazite inclusions in the reacted fluorapatite. The monazite inclusions have no amorphous rims, show what appears to be a pseudo-hexagonal symmetry, and are in direct contact with the fluorapatite. **b** shows a HRTEM image of one of the nano-void channels as a distortion of the lattice fringes in the vicinity of the nano-void channel

the grain rim. This would then hinder the exchange of the fluid inside the grain, i.e. in the nano-channels, with the fluid outside the grain. As a result, the mobility of the reaction front is reduced. At the same time, the concentration of (Y + REE) at the reaction front would continue to increase as more of the original (Y + REE)-rich fluorapatite is converted to (Y + REE)-depleted fluorapatite. At some point during the experiment, the concentration of (Y + REE) in these fluids would reach supersaturation such that monazite nucleation and growth becomes possible, but only at or very close to the reaction front.

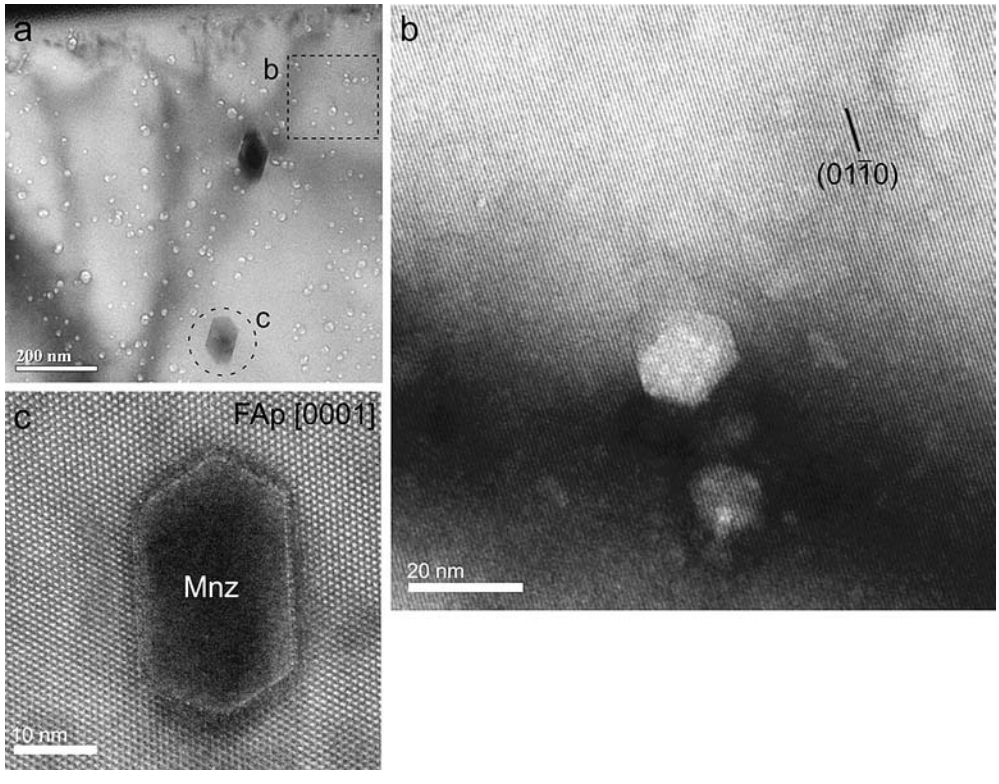

Fig. 12 **a** shows a TEM bright field image from foil 3 (AM31; Fig. 3b) showing numerous nano-voids (or nano-pores). **b** shows a lattice fringe image of a field of nano-voids from the same TEM foil. Note the inverted hexagonal symmetry of the numerous nano-voids scattered throughout the thickness of the TEM foil. **c** shows an HRTEM image of one of the monazite inclusions. Here, the zone axis of the fluorapatite is [0001]. Note the lack of an amorphous rim at the grain boundary interface between the monazite inclusion and the surrounding fluorapatite similar to what is seen for some of the monazite inclusions in Fig. 6. Also note the apparent, pseudo-hexagonal symmetry of the monazite inclusions in Figs. 6a and c

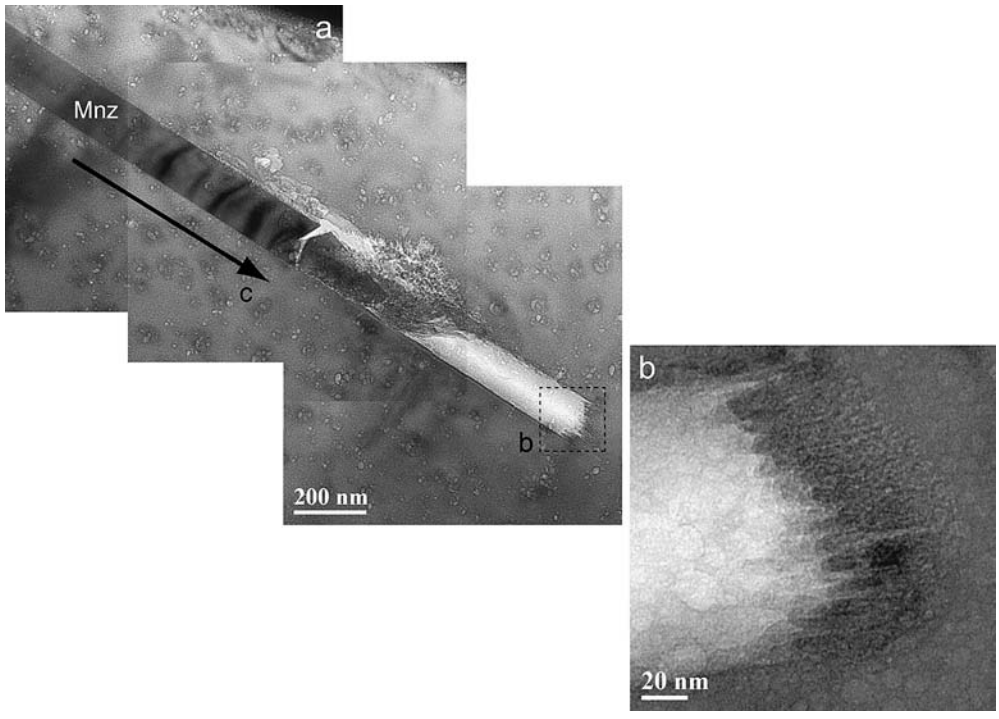

Fig. 13 **a** shows an elongated monazite inclusion in TEM foil 1 (AM31: Fig. 2b). The monazite inclusion is surrounded by numerous nano-voids. It appears to be growing into what was once a fluid-filled void. At the end of the formerly fluid-filled void, a transition region is visible with numerous small spike-like features (Fig. 13b). These spikes appear to represent highly localised regions of preferred dissolution, no more than 5 nm in diameter, which are advancing along the fluorapatite *c*-axis as the fluid-filled void and subsequent elongated monazite inclusion extend and grow within the fluorapatite. Here, the crystallographic orientation of the fluorapatite determines the shape of the monazite inclusion

H_2SO_4 reaction experiments

Compared to the HCl experiments, those involving H_2SO_4 were more sluggish requiring either longer reaction times, higher concentrations of H_2SO_4, or higher temperatures to achieve both reaction of the fluorapatite with the acid as well as the formation of monazite inclusions (Table 1). In addition, recrystallisation of fluorapatite in the reacted regions never occurred. The fact that the chemical boundary between some of the reacted and unreacted regions in one particular experiment, i.e. AM31 (1 N H_2SO_4; 900°C; 1,000 MPa) (Fig. 3a, b), is diffuse rather than sharp (Figs. 3a, b, 4), indicates that, in addition to dissolution–reprecipitation, volume diffusion may have also played a role along some of the reaction fronts. This is in contrast to experiments, which involve either a greater concentration of H_2SO_4, e.g. AM44 (2 N H_2SO_4; 600°C; 500 MPa) (Fig. 3c) or have a greater reaction time, albeit at considerably lower temperatures, e.g. AM42 (1 N H_2SO_4; 300°C; 500 MPa) (Fig. 3d, e). In either experiment, the complete lack of diffuse reaction boundaries signals either higher reactivity (e.g. AM44) or temperatures at which volume diffusion is negligible relative to dissolution–reprecipitation (e.g. AM42).

Foil 2, cut on the extreme rim of the fluorapatite grain from experiment AM31, indicates the presence of 10–20 nm wide nano-channels (Fig. 11). Further in, the reacted region is dominated by numerous, individual

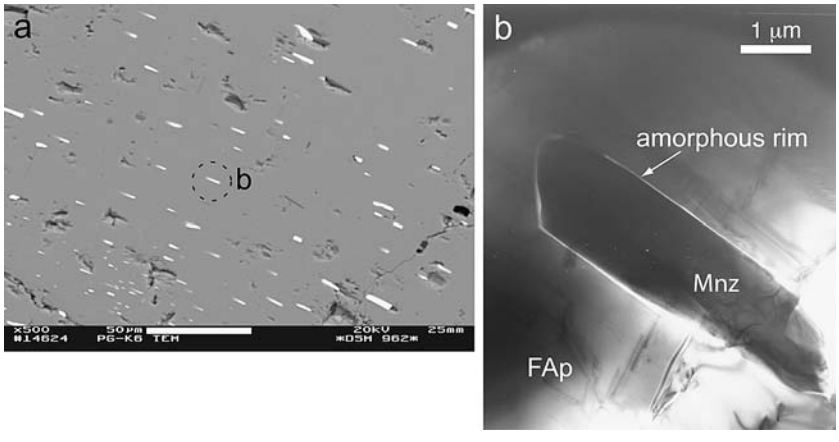

Fig. 14 **a** shows a BSE image of elongated monazite inclusions in fluorapatite from the Kirunavaara fluorapatite–magnetite ore deposit, N. Sweden (Harlov et al. 2002b). The monazite inclusions are conjectured to have resulted from auto-metasomatism. **b** shows a TEM bright field image of one of these monazite inclusions with

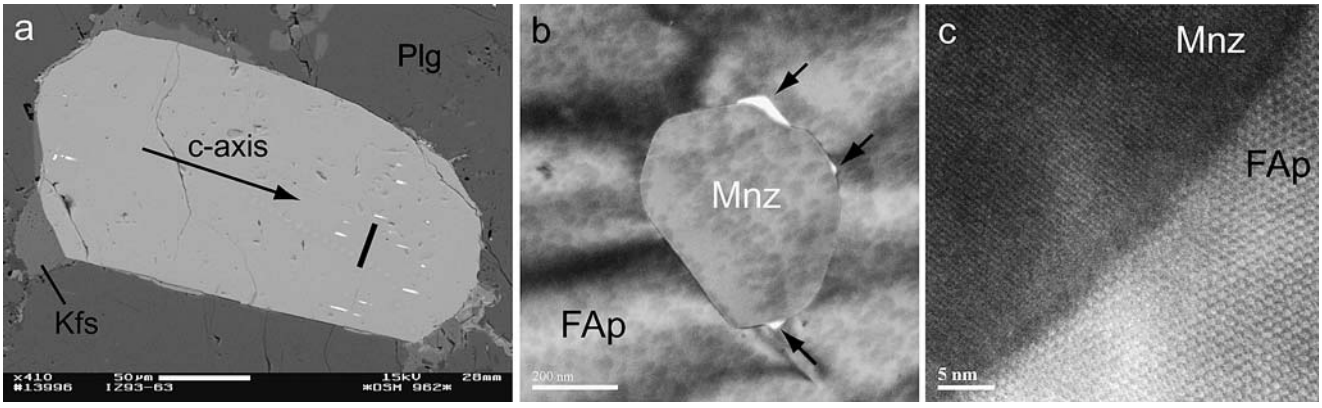

Fig. 15 **a** shows a BSE image of a fluorapatite grain from a granulite-facies metabasite located in the Val Strona traverse of the Ivrea-Verbano Zone, N. Italy (Harlov and Förster 2002). Here, metasomatically induced, elongated monazite inclusions are seen scattered within the grain interior. The arrow indicates the approximate direction of the fluorapatite *c*-axis. The location, where the TEM foil was cut, is indicated by the *black bar*. **b** shows a TEM bright field image of a cross section of one of the monazite inclusions. Note the lack of an amorphous rim at the grain boundary interface between the monazite inclusion and the surrounding fluorapatite. Instead, there are several randomly located voids along this interface (designated by *arrows*). This lack of an amorphous rim is confirmed in the HRTEM image of the monazite-fluorapatite grain boundary interface in (**c**)

nano-voids, which give the fluorapatite a faint, sponge-like appearance (Figs. 12, 13). This might imply an evolutionary pattern, in which the dispersed nano-voids evolve into nano-channels, though only on the very edges of the fluorapatite grains or those regions that have experienced the longest period of reactivity with the 1 N H_2SO_4 solution. With regard to the nano-voids, it is difficult to ascertain their interconnectivity from a two-dimensional TEM foil. However, the void associated with the elongated monazite grain in Fig. 13 was formerly filled with fluids. This would suggest that growth of the monazite inclusion was supplied via these nano-voids implying that they must be interconnected. Such an argument would be further supported by the presence of other monazite inclusions in the reacted regions (Figs. 11a, 12a, c). Similar to what is seen in the HCl experiments, penetration of fluids would enhance mass transfer of (Y + REE) and Ca, possibly as sulphates, and P as phosphoric acid (H_3PO_4), and thereby aid in the nucleation and growth of monazite inclusions.

The remaining monazite inclusions sampled in these TEM foils show no evidence of any type of associated void or amorphous rim (e.g. Fig. 12c). This would imply that their rate of growth was either co-equal with the dissolution of the surrounding fluorapatite or else, the monazite has grown such that it has filled in the former, fluid-filled nano-void space. The latter idea is supported by the observation that these particular monazite inclusions tend to have hexagonal shapes reminiscent of the inverted hexagonal symmetry typical of the nano-voids in this region (cf. Figs. 12b, c).

Physical and chemical change during dissolution–reprecipitation

Dissolution–reprecipitation has been commonly observed in other minerals, both from nature (Putnis 2002; Tomaschek et al. 2003) as well as experimentally (e.g. Yanagisawa et al. 1999; Rendón-Angeles et al. 2000a, b; Putnis 2002; Hellmann et al. 2003; Putnis and Mezger 2004; Labotka et al. 2004; Pollack et al. 2004a,b). However, it should be noted that creation of a pervasive micro-porosity in a mineral is not limited only to dissolution–reprecipitation, but may also be due to a simple change in volume between the original and reacted material during some physical event such as metasomatism or annealing (e.g. Harlov et al. 2002a, their Fig. 6c; Geisler et al. 2004).

In the case of the fluorapatite-HCl–H_2SO_4 experiments, porosity is mostly on the nano-scale, except at low temperatures, i.e. 300°C (cf. Figs. 1f, 3d, e). In addition, the reacted region has retained the same crystallographic orientation as the original, unreacted fluorapatite (Fig. 7c). This is because the reacted fluorapatite has not been recrystallised, but rather represents a replacement or reprecipitation. Here, the (Y + REE)-depleted fluorapatite, replacing the (Y + REE)-rich fluorapatite, utilises the original unreacted crystal as a template. This would argue for calling such a replacement a topotaxial one since the newly reprecipitated phase is still fluorapatite with the same crystal structure and crystallographic orientation as the original, (Y + REE)-rich fluorapatite (see also discussion in Yanagisawa et al. 1999). In this particular case, any lattice mismatch between the reacted and unreacted fluorapatite could easily be compensated for by dislocations in the crystal lattice of the reacted fluorapatite.

Because dissolution–reprecipitation normally is associated with a change in chemical composition, it represents a reaction, which is characterized by a change in the Gibbs free energy. It is this change in the Gibbs free energy, which drives the dissolution–reprecipitation process. In these particular experiments, the reaction represented consists of converting a higher lattice energy, (Y + REE + Si + S + Na + Cl)-rich fluorapatite to a

lower lattice energy fluorapatite depleted in these elements.

In the HCl experiments, propagation of the reaction or infiltration front into the (Y + REE)-rich fluorapatite during the dissolution–reprecipitation process appears to consist of extending the fluid-filled nano-channels across the reaction front while, at the same time, the termination of each nano-channel shows some limited migration over the two-dimensional surface of the reaction front. In contrast, in the H_2SO_4 experiments, propagation appears to be principally due to the forward migration of the nano-voids, coupled with some volume diffusion under certain temperatures and concentrations of H_2SO_4.

Dissolution–reprecipitation is also highly dependent upon the reactivity of either acid. Once this reactivity has been diminished, either by recrystallisation of the nano-channels, thereby blocking access of the reaction front to outside fluids and/or a decrease in the reactivity of the acid due to a build-up of other components from the reacted fluorapatite, forward propagation apparently either stops or else moves so slowly as to not be detectable over experimental time scales. Volume diffusion would then predominate at the reaction front, though only if the rate of dissolution–reprecipitation is relatively slower.

The nano-voids and nano-channels play an important role by serving as sites for nucleation and growth of the monazite inclusions both at the reaction front (e.g. Fig. 6a) as well as behind it (Figs. 7a, 11, 12, 13). Monazite formation does not involve exsolution from a solid solution, but rather is the fluid-aided growth of a separate phase, which utilises the materials immediately at hand. Such growth may be referred to as topotactic-like (see discussion in Pan et al. 1993) since the formation and growth of one phase (i.e. monazite), within a second phase (i.e. fluorapatite) can be required to adjust to the surrounding crystallography of the second phase such as seen in the H_2SO_4 experiments (e.g. Figs. 11a, 12a, c, 13a). In other cases, the monazite grains may grow in a random orientation as long as they have no or only partial contact with the surrounding fluorapatite as seen in the HCl experiments, i.e. a fluid film separates the monazite from the fluorapatite (e.g. Fig. 7d). Whether topotactic-like growth of monazite in fluorapatite will occur appears to be a direct function of the reactivity of the fluid responsible for initiating the dissolution–reprecipitation process in fluorapatite.

Implications for mineral equilibration and fluid transport

In rocks, equilibration, in the form of mass transfer between minerals, is greatly enhanced by the presence of fluids along grain boundaries. If the fluid, e.g. brines (cf. Holness 1997; Gibert et al. 1998), has a relatively low wetting angle, it will form an interconnected network along grain boundaries. As a consequence, it could then be possible for equilibration to be achieved on a scale ranging from centimetres to meters to even kilometres over geological time scales (Newton et al. 1998).

One consequence of fluids along grain boundaries could be dissolution–reprecipitation of the grain rims, especially if such fluids contain chemical components that are relatively reactive with the surrounding minerals. Putnis (2002) has documented studies of dissolution–reprecipitation in a number of minerals such as feldspars, feldspathoids, apatite, aluminosilicates, zircon (see also Tomaschek et al. (2003)), sulphides, and salts such as KCl-KBr. The results of this study first confirm that dissolution–reprecipitation, both on the nano- and micro-scale, has occurred in fluorapatite. More importantly, they demonstrate how the fluids permeating the resultant porosity can greatly aid in mass transfer and thus allow for the nucleation and growth of one mineral phase (monazite) inside a second mineral phase (fluorapatite). The implication from these observations, applied to rocks in general, is that if fluids exist along grain boundaries, they could also exist 10s to 100s of microns within grain rims in the nano- and micro-porosity resulting from dissolution–reprecipitation. If true, such a phenomenon would greatly expand fluid pathways in rocks and thus would allow for much greater volumes of fluid to penetrate the rock than would be possible only along the grain boundaries.

As to how permanent such a porosity would be is uncertain. One might conjecture that its presence would be a direct function of fluid reactivity coupled with fluid volume. During those times, when there were only very small amounts of fluid present or fluids were totally absent along grain boundaries, it is probable that this micro- and nano-porosity within the grain rims would disappear due to recrystallisation, only to reappear during the next fluid influx. When fluids were effectively absent, equilibration between minerals could then only take place by volume diffusion. This would explain why minerals in rocks, which have remained relatively dry during metamorphism, tend to be in disequilibrium. One example of how fluids can facilitate mineral equilibration during metamorphism has been documented by Wain et al. (2001). In this particular example, rocks of apparent granulite grade (900–1,100 MPa; 700–800°C) in the Western Gneiss region of Norway have been taken to eclogite-facies (2,000–2,300 MPa; 650–850°C). This event is recorded in approximately 5% of the complex, which has been converted to eclogite in zones of fluid infiltration and deformation. The remaining dry, granulite-facies rocks show no indication at all, either from the mineral chemistry or reaction textures, of ever having experienced eclogite-facies metamorphism.

In retrospect, porous grain rims probably would not survive the millions to 10s of millions of years of metamorphic uplift and cooling. Instead, they would have long since been recrystallised in a manner similar to what is seen in the reacted regions in fluorapatite grains from the HCl experiments (compare Figs. 9 and 10). Evidence that such a porosity in the grain rims previ-

ously existed could take the form of higher concentrations of fluid inclusions, the presence of mineral inclusions for which no thermodynamic or physical evidence exists that the inclusion is either (1) a product of solid state exsolution or (2) has been overgrown during growth of the host mineral phase, and/or a crystallographic lattice, which shows general signs of having been disturbed and later healed to a mosaic crystal pattern similar to what is documented in Fig. 9.

The fact that in nature, monazite inclusions are found distributed throughout metasomatised fluorapatite (Harlov and Förster 2002, 2003; Harlov et al. 2002b) and chlorapatite (Harlov et al. 2002a) has already been demonstrated to be a strong indication that both types of apatite have been transformed to new compositions via dissolution–reprecipitation that involved complete infiltration by fluids during metasomatism. The results from this study confirm this conclusion. By analogy, these results could be applied to studies of other rock-forming minerals during metasomatism, e.g. the feldspars (see examples in Putnis 2002, also O'Neil 1977). The implication then is that, given sufficient fluid resources and time, total recrystallisation of mineral phases, via dissolution–reprecipitation, could represent one means by which minerals re-equilibrate in a rock during metamorphism. More to the point, dissolution–reprecipitation would allow for increased fluid penetration along grain boundaries, which could help to promote mass transfer along the rock column as material is brought in and removed. In that respect, fluid-rock interaction, on either the local or more regional scale, would then not just be a simple matter of fluid flow along grain boundaries, but fluid flow through grain boundaries or even through the minerals themselves, thereby allowing for both mineral equilibrium and mass transfer on a scale far grander than has so far been conceptualised.

Acknowledgements Jan Lindsey is thanked for providing the crystal of the Durango fluorapatite used in this study, which she collected on excursion to Durango, Mexico. We thank Dieter Rhede and Oona Appelt for support with the microprobe. Helga Kemnitz is acknowledged for assistance with the SEM. Killian Pollack, Andrew Putnis, and Rainer Abart are thanked for useful discussions. Roland Hellman is thanked for critically reading an earlier version of this manuscript. Joe Pyle, Thorsten Geisler, and Franck Poitrasson are thanked for their insightful and helpful reviews, which greatly helped to clarify and improve the manuscript.

References

Åmli R (1975) Mineralogy and rare earth geochemistry of apatite and xenotime from the Gloserheia Granite Pegmatite, Froland, southern Norway Am Mineral 60:607–620

Cherniak DJ (2000) Rare earth element diffusion in apatite Geochim Cosmochim Acta 64:3871–3885

Geisler T, Seydoux-Guillaume A-M, Wiedenbeck M, Wirth R, Berndt J, Zhang M, Mihailova B, Putnis A, Salje EKH, Schlüter J (2004) Periodic precipitation pattern formation in hydrothermally treated metamict zircon Am Mineral 89:1341–1347

Gibert F, Guillaume D, Laporte D (1998) Importance of fluid immiscibility in the H_2O-NaCl-CO_2 system and selective CO_2 entrapment in granulites: experimental phase diagram at 5–7 kbar, 900°C and wetting textures Eur J Mineral 10:1109–1123

Harlov DE, Förster H-J (2002) High-grade fluid metasomatism on both a local and regional scale: the Seward Peninsula, Alaska and the Val Strona di Omegna, Ivrea-Verbano zone, northern Italy. Part II: Phosphate mineral chemistry J Petrol 43:801–824

Harlov DE, Milke R (2002) Stability of corundum + quartz relative to kyanite and sillimanite at high temperature and pressure Am Mineral 87:424–432

Harlov DE, Förster H-J, Nijland TG (2002a) Fluid-induced nucleation of REE-phosphate minerals in apatite: nature and experiment. Part I. Chlorapatite Am Mineral 87:245–261

Harlov DE, Andersson UB, Förster H-J, Nyström JO, Dulski P, Broman C (2002b) Apatite-monazite relations in the Kiirunavaara magnetite-apatite ore, northern Sweden Chem Geol 191:47–72

Harlov DE, Förster H-J (2003) Fluid-induced nucleation of REE-phosphate minerals in apatite: nature and experiment. Part II. Fluorapatite Am Mineral 88:1209–1229

Hellmann R, Penisson J-M, Hervig RL, Thomassin J-H, Abrioux M-F (2003) An EFTEM/HRTEM high-resolution study of the near surface of labradorite feldspar altered at acid pH: evidence for interfacial dissolution-reprecipitation Phys Chem Minerals 30:192–197

Holness MB (1997) Surface chemical controls on pore-fluid connectivity in texturally equilibrated materials. In: Jamtveit B, Yardley BWD (eds) Fluid flow and transport in rocks Chapman and Hall, London, pp 149–169

Jarosewich E, Boatner LA (1991) Rare-earth element reference samples for electron microprobe analysis Geostand Newslet 15:397–399

Johannes W, Bell PM, Mao HK, Boettcher AL, Chipman DW, Hays JF, Newton RC, Seifert F (1971) An interlaboratory comparison of piston-cylinder pressure calibration using the albite-breakdown reaction Contrib Mineral Petrol 32:24–38

Johannes W (1973) Eine vereinfachte Piston-Zylinder-Apparatur hoher Genauigkeit N Jb Mineral 1973:337–351

Labotka TC, Cole DR, Fayek M, Riciputi LR, Stadermann FJ (2004) Coupled cation and oxygen-isotope exchange between alkali feldspar and aqueous chloride solution Am Mineral 89:1822–1825

Lyons JI (1988) Volcanogenic iron oxide deposits, Cerro de Mercado and vicinity, Durango Mexico. Econ Geol 83:1886–1906

Newton RC, Aranovich LYa, Hansen EC, Vandenheuvel BA (1998) Hypersaline fluids in Precambrian deep-crustal metamorphism Precamb Res 91:41–63

O'Neil JR (1977) Stable isotopes in mineralogy. Phys Chem Minerals 2:105–123

Pan Y (1997) Zircon- and monazite-forming metamorphic reactions at Manitouwadge, Ontario Can Mineral 35:105–118

Pan Y, Fleet ME, Macrae ND (1993) Oriented monazite inclusions in apatite porphyroblasts from the Hemlo gold deposit, Ontario, Canada Mineral Mag 57:697–707

Pan Y, Fleet ME (2002) Composition of the apatite-group minerals: substitution mechanisms and controlling factors. In: Kohn MJ, Rakovan J, Hughes JM (eds) Phosphates: geochemical, geobiological, and materials importance, 48:13–49. Reviews in Mineralogy, Mineralogical Society of America, Washington, DC

Pollack K, Geisler T, Putnis A (2004a) How does a replacement front proceed? Observations on chlorapatite-hydroxylapatite replacements Geochim Cosmochim Acta 68:A184

Pollack K, Geisler T, Putnis A (2004b) The replacement of chlorapatite by hydroxylapatite under hydrothermal conditions: mechanisms and kinetics of re-equilibration Beih Eur J Mineral 16:107

Putnis A (2002) Mineral replacement reactions: from macroscopic observations to microscopic mechanisms Mineral Mag 66:689–708

Putnis CV, Mezger K (2004) A mechanism of mineral replacement: Isotope tracing in the model system KCl-KBr-H_2O Geochim Cosmochim Acta 68:2839–2848

Rendón-Angeles JC, Yanagisawa K, Ishizawa N, Oishi S (2000a) Effect of metal ions of chlorapatite on the topotaxial replacement by hydroxylapatite under hydrothermal conditions J Solid State Chem 154:569–578

Rendón-Angeles JC, Yanagisawa K, Ishizawa N, Oishi S (2000b) Topotaxial conversion of chlorapatite and hydroxylapatite to fluorapatite by hydrothermal ion exchange Chem Material 12:2143–2150

Stormer JC, Pierson ML, Tacker RC (1993) Variation of F and Cl X-ray intensity due to anisotropic diffusion in apatite during electron microprobe analysis Am Mineral 78:641–648

Tomaschek F, Kennedy AK, Villa IM, Lagos M, Ballhaus C (2003) Zircons from Syros, Cyclades, Greece–Recrystallization and mobilization of zircon during high-pressure metamorphism. J Petrol 44:1977–2002

Yanagisawa K, Rendon-Angeles JC, Ishizawa N, Oishi S (1999) Topotaxial replacement of chlorapatite by hydroxylapatite during hydrothermal ion exchange Am Mineral 84:1861–1869

Young EJ, Myers AT, Munson EL, Conklin NM (1969) Mineralogy and geochemistry of fluorapatite from Cerro de Mercado, Durango, Mexico US Geological Survey Professional Paper 650(D):D84–D93

Wain AL, Waters DJ, Austrheim H (2001) Metastability of granulites and processes of eclogitisation in the UHP region of western Norway J Met Geol 19:609–625

Wirth R (1997) Water in minerals detectable by electron energy loss spectroscopy EELS Phys Chem Minerals 24:561–568

Wirth R (2004) Focused ion beam (FIB): A novel technology for advanced application of micro- and nanoanalysis in geosciences and applied mineralogy Eur J Mineral 15:863–875